Sandeep Khanduri, 2026, 14:3
ISSN (Online): 2348-4098
ISSN (Print): 2395-4752

International Journal of Science, Engineering and Technology
An Open Access Journal

Voltage Stabilization of A DC Microgrid Feeding an EV Charging Station Using a Systematically Tuned Fractional-Order Controller

Sandeep Khanduri[1], Dr. Himanshu Maithani[2], Dr Charu[3]
Dev Bhoomi Uttarakhand University, Dehradun[12]
Quantum University, Roorkee[3]

Abstract- High-power electric vehicle (EV) fast charging causes problems like CPL behavior, which destabilizes DC microgrids because of negative incremental impedance. In this paper, a control scheme for DC bus voltage stabilization in an EV integrated DC microgrid based on a fractional-order proportional integral derivative (FOPID) control approach has been proposed. First, a nonlinear averaged modeling considering boost converter dynamics and the characteristic of CPL is performed. Then, linearized small signal models are used to investigate the limits of stability along with critical parameters. A multi-objective tuning approach is then employed to tune a PI, PID, and FOPID controller under the same operation conditions. The performance comparison has been done in the time domain, frequency domain, sensitivity analysis, and nonlinear disturbance analysis. It is concluded that FOPID controller performs better than PID and PI in terms of phase margin, disturbance rejection, and robustness, while providing a good compromise in other parameters.

Keywords: DC microgrid, electric vehicle charging station, constant power load, fractional-order control, FOPID controller, voltage regulation, robustness analysis.

I. INTRODUCTION

Electrification of the transport system has transitioned from a goal to be achieved through policies to become a major engineering revolution in today's power systems. The swift development of fast charging facilities for EVs, mostly in cities and highway networks, brings a whole new challenge to grid networks because of the dynamic stress being brought to them. It becomes more efficient and easier to implement a DC microgrid structure due to its ability to integrate easily with renewable energy resources, energy storages, and DC-based charging stations [1]-[6].

DC microgrids also overcome some of the weaknesses of conventional AC microgrids in terms of synchronization issues and multiple conversion stages that make it less effective and inefficient. The downside of using DC microgrids is that it results in lower intrinsic stability and greater sensitivity to disturbances in the loads. Charging facilities for high-power EVs are usually capable of generating hundreds of kilowatts to megawatts of charging powers per station [6]-[11]. An essential aspect of EV fast chargers is their Constant Power Load (CPL) characteristics. Upon connection to the network, EV fast chargers try to maintain the constant charging power regardless of the DC bus voltage level changes. This leads to a phenomenon called negative incremental impedance behavior, a well-known cause of instability within DC power systems [12]-[19]. Negative impedance characteristics can lead to

- Reduced damping,
- Oscillatory voltage behavior,
- Hopf bifurcation under heavy loading,
- Potential collapse of DC bus voltage.

Conventional PI and PID controllers remain the dominant industrial solution for DC bus regulation due to their simplicity, maturity, and ease of implementation [20]-[23]. But the use of integer order controllers limits their capacity to manipulate the dynamic behavior of the system, especially during the operation with nonlinear control plants. Their constant slopes for integration and differentiation limit their ability to manipulate phase. The use of fractional-order control involves

extending the conventional concepts of integer order control theory to include arbitrary real orders. The FOPID, which is a fractional order extension of the PID controller, includes the addition of two new design parameters lambda and mu [24]-[26].

Importantly, fractional-order systems exhibit memory-dependent behavior, which can improve suppression of oscillations induced by CPL dynamics.

Despite promising results reported in power electronics, DC-microgrid voltage regulation, and fractional-order controller tuning studies [21]-[26], many studies applying fractional-order controllers to DC microgrids still require clearer comparative validation under high-power EV charging conditions. In particular, comparative studies should show how controller tuning affects transient response, frequency-domain margins, disturbance rejection, and robustness under parameter variation.

This paper therefore focuses on a simulation-validated fractional-order control framework. The contribution is built around nonlinear modeling, linearized plant analysis, FOPID controller formulation, transparent tuning, and comparative validation against PI and PID controllers.

Existing studies usually treat controller tuning, CPL stabilization, converter small-signal analysis, and EV fast-charging robustness as separate problems. Few studies evaluate PI, PID, and FOPID on the same EV-charging DC microgrid while simultaneously enforcing duty-ratio feasibility, finite gain and phase margins, peak-sensitivity limits, nonlinear disturbance recovery, and +/-20 percent parameter variation. The novelty of this work is therefore the unified constrained multi-objective comparison framework, rather than the isolated use of a fractional-order controller.

This directly addresses the gap between fractional-order tuning studies and practical robustness requirements for CPL-dominated EV charging stations [39]-[43].

THE MAJOR CONTRIBUTIONS OF THIS WORK ARE SUMMARIZED AS FOLLOWS:

The novelty of this research is highlighted by integrating the concepts of non-linear CPL dynamics, EV fast-charging phenomena, and multi-metric normalized performance evaluation into a comparative control study.

Non-linear modeling of EV-integrated DC micro-grid: An average model that considers the effect of boost converter dynamics, CPL characteristics, and EV fast-charging is formulated for both linear and non-linear studies.

Formulation of fractional-order controller:

The $PI^{\lambda} \times D^{\mu}$ controller is designed based on a rational approximation suitable for simulation.

Frequency domain analysis: The comparison among PI, PID, and FOPID controllers is based on step response, finite gain-margin Bode plot, sensitivity function, and pole-zero map analysis.

Tuning of controllers under constraints: Parameters of PI, PID, and FOPID controllers are chosen through a constrained iteration method based on transient response, finite gain margin, phase margin, duty cycle, disturbance rejection, and robustness.

Robustness evaluation:

Controller robustness is determined through the implementation of parameter variation tests and load disturbance simulations. The final result of the comparison will be presented using a multi-criteria normalization scheme.

The rest of the paper is structured as follows. Section II presents the nonlinear model of the DC microgrid and EV charger. Section III proposes the design of the fractional order controller. Section IV discusses the concept of linearization for design purpose. Section V introduces the tuning process. Finally, the results are presented in Section VI. Section VII concludes the paper.

II. NONLINEAR MODELING OF DC MICROGRID AND EV CHARGING STATION:

The dynamic behavior of a DC microgrid feeding a high-power EV charging station is fundamentally governed by power electronic converter dynamics and the nonlinear characteristics of the constant power load (CPL). In this section, a complete nonlinear averaged model is derived. The analysis explicitly captures the destabilizing effect introduced by CPL behavior and forms the foundation for controller design and stability analysis in subsequent sections.

System Configuration:

The considered DC microgrid architecture consists of:

- A DC source (renewable source or upstream DC link),
- A boost-type DC–DC converter,
- A centralized DC bus capacitor,
- A high-power EV charger modeled as a constant power load.

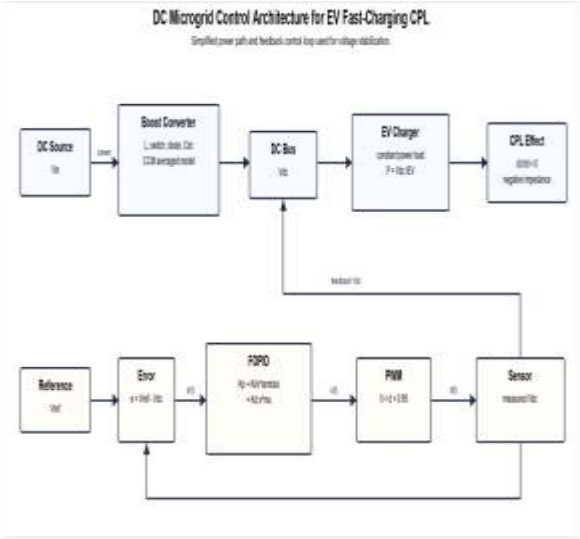

Fig. 1. Simplified control architecture of the DC microgrid with boost converter and constant power load (CPL).

The system consists of renewable generation, a bidirectional DC-DC converter, a centralized DC bus capacitor, and an EV charger modeled as a constant power load (CPL). The FOPID controller regulates the duty cycle to maintain DC bus voltage stability under load disturbances.

This configuration follows common DC microgrid and EV fast-charging station architectures reported in recent review and station-design studies [5], [6], [11]. The simplified structure is shown in Fig. 1. The converter regulates the DC bus voltage to a reference value despite disturbances caused by EV charging demand.

Table 1: Key Technical Challenges in EV-Integrated DC Microgrids

Challenge	Physical Cause	Control Implication
Negative incremental impedance	Constant power load behavior	Reduced damping and oscillations
Low system inertia	Converter-dominated architecture	Fast transient instability
Step-load disturbances	Plug-in events of EV chargers	Voltage overshoot or undershoot
Parameter uncertainty	Line impedance and battery dynamics	Robustness requirement

B. Nonlinear Averaged Boost Converter Model

To avoid switching-level complexity, we adopt an averaged continuous-conduction-mode boost-converter model, which is widely used for charger-interface and high-power DC-DC converter analysis [7], [8].

Let:

The principal symbols used in the nonlinear model are listed as follows:

- iL = inductor current
- vdc = DC bus voltage
- Vin = input voltage
- L = inductance
- C = capacitance
- d = duty ratio
- iEV = EV current

1) Inductor Dynamics

Applying Kirchhoff's Voltage Law (KVL):

$$L\frac{di_L}{dt} = V_{in} - (1-D)V_{dc} \qquad (1)$$

2) DC Bus Capacitor Dynamics

Applying Kirchhoff's Current Law (KCL):

$$C_{dc}\frac{dV_{dc}}{dt} = (1-D)i_L - i_{load} \qquad (2)$$

Equations (1–2) form the nonlinear state equations of the boost converter.

C. EV Charger as Constant Power Load (CPL)

Fast EV chargers operate under nearly constant power regulation during the constant-current or constant-power charging phase [19]. Therefore, the EV load can be modeled as:

$$P_{EV} = V_{dc} i_{load} \qquad (3)$$

Thus,

$$i_{load} = \frac{P_{EV}}{V_{dc}} \qquad (4)$$

Substituting (4) into (2):

$$C_{dc}\frac{dV_{dc}}{dt} = (1-D)i_L - \frac{P_{EV}}{V_{dc}} \qquad (5)$$

Equations (1) and (5) define the complete nonlinear dynamics.

D. Negative Incremental Impedance of CPL

The destabilizing nature of the CPL can be observed by computing its incremental impedance:

$$Z_{inc} = \frac{dV_{dc}}{di_{load}}$$

Differentiating (4):

$$\frac{di_{load}}{dV_{dc}} = -\frac{P_{EV}}{V_{dc}^2}$$

Thus,

$$Z_{inc} = \left(\frac{di_{load}}{dV_{dc}}\right)^{-1} = -\frac{V_{dc}^2}{P_{EV}} \qquad (6)$$

Equation (6) shows negative incremental impedance. Physically, this implies:

- A decrease in bus voltage increases load current.
- A voltage disturbance is amplified rather than damped.

This negative damping effect is the primary cause of oscillatory instability in DC microgrids with CPLs [20, 21].

E. Nonlinear State-Space Representation

Define state vector:

$$x = \begin{bmatrix} i_L \\ V_{dc} \end{bmatrix}$$

Control input:

$$u = D$$

From (1) and (5):

$$\dot{x}_1 = \frac{1}{L}(V_{in} - (1-u)x_2) \qquad (7)$$

$$\dot{x}_2 = \frac{1}{C_{dc}}\left((1-u)x_1 - \frac{P_{EV}}{x_2}\right) \qquad (8)$$

Equations (7)–(8) constitute the nonlinear state-space model:

$$\dot{x} = f(x,u) \qquad (9)$$

The system is nonlinear due to:

- Multiplicative coupling term ux_2
- Rational term P_{EV}/x_2

F. Equilibrium Point Computation

At steady state:

$$\dot{x}_1 = 0, \dot{x}_2 = 0$$

From (7):

$$V_{in} = (1-D_0)V_0 \qquad (10)$$

From (8):

$$(1-D_0)I_0 = \frac{P_{EV}}{V_0} \qquad (11)$$

Solving (10):

$$D_0 = 1 - \frac{V_{in}}{V_0} \qquad (12)$$

From (11):

$$I_0 = \frac{P_{EV}}{(1-D_0)V_0} \qquad (13)$$

The equilibrium exists only if:

$$P_{EV} < P_{max}$$

where P_{max}depends on converter ratings and input voltage.

G. Small-Signal Linearization

Let perturbations:

$i_L = I_0 + \hat{i}$
$V_{dc} = V_0 + \hat{v}$
$D = D_0 + \hat{d}$

Linearizing (7) and (8) around equilibrium:
1) Inductor Equation

$$L\frac{d\hat{i}}{dt} = -(1 - D_0)\hat{v} + V_0\hat{d} \qquad (14)$$

2) Capacitor Equation
Using Taylor expansion:
$\frac{P_{EV}}{V_{dc}} \approx \frac{P_{EV}}{V_0} - \frac{P_{EV}}{V_0^2}\hat{v}$

Substituting:

$$C_{dc}\frac{d\hat{v}}{dt} = (1 - D_0)\hat{i} - I_0\hat{d} + \frac{P_{EV}}{V_0^2}\hat{v} \qquad (15)$$

H. Linear State-Space Model
The linearized model becomes:

$$\dot{\hat{x}} = A\hat{x} + B\hat{d} \qquad (16)$$

where

$$A = \begin{bmatrix} 0 & -\frac{1 - D_0}{L} \\ \frac{1 - D_0}{C_{dc}} & \frac{P_{EV}}{C_{dc}V_0^2} \end{bmatrix} \qquad (17)$$

$$B = \begin{bmatrix} \frac{V_0}{L} \\ -\frac{I_0}{C_{dc}} \end{bmatrix} \qquad (18)$$

I. Open-Loop Stability Analysis
The characteristic equation is:
$\det(sI - A) = 0$

$$s^2 - \left(\frac{P_{EV}}{C_{dc}V_0^2}\right)s + \frac{(1-D_0)^2}{LC_{dc}} = 0 \qquad (19)$$

Observe that the coefficient of s is positive:

$$a_1 = -\frac{P_{EV}}{C_{dc}V_0^2}$$

For large P_{EV}, one root moves toward the right-half plane.

Thus, as EV charging power increases, the system can lose stability even without control delay.
This explains why classical control methods must be carefully designed in CPL-dominated systems.

J. Critical Power Condition
Applying Routh–Hurwitz condition:
For stability:

$$\frac{P_{EV}}{C_{dc}V_0^2} < 2\sqrt{\frac{(1-D_0)^2}{LC_{dc}}}$$

Thus, the maximum allowable EV power is:

$$P_{crit} = 2V_0^2(1 - D_0)\sqrt{\frac{C_{dc}}{L}} \qquad (20)$$

If $P_{EV} > P_{crit}$, the open-loop system becomes unstable.
This motivates the need for robust voltage regulation.

Since a1 < 0 when P_EV > 0, an ideal model that has no losses cannot provide us with a positive open-loop critical power limit. It would require adding some kind of damping factors, such as parasitic resistances, line resistances, dynamic source impedance, or active closed-loop damping for the finite critical gain limit to be calculated.

For that reason, the critical curve that was chosen for controller motivation must be regarded as qualitative only. The more EVs are charged by power converters, the higher is the demand for damping and voltage control.

In stability design, the negative coefficient of the first order in Equation (18) shows that the plant without any damping is unstable for CPL operation mode. Hence, the function of the controller must consist in adding the damping action into the open-loop duty ratio channel without violating the realistic duty ratio constraints. Though the complete Lyapunov proof lies beyond the scope of the current comparative simulation analysis, the selected controller was tested not on the step-response alone but through finite gain margins, phase margins, peaks of sensitivity, nonlinear recoverability, and 20 percent variation envelopes.

Table 2. System Parameters Used for Analysis

Parameter	Symbol	Typical Value

Inductance	L	2 mH
DC bus capacitance	Cdc	2200 uF
Nominal voltage	V0	400 V
EV charging power	PEV	50-150 kW
Input voltage	Vin	250 V

The above-mentioned nonlinear analysis demonstrates that:

- 1.The presence of CPL results in destabilizing positive feedback.
- 2.The stability margin decreases with increase in power generated by EV charging.
- 3.For an open-loop DC microgrid to be stable in presence of CPL, active damping is essential.
- 4.Controller design should counteract negative incremental impedance.
- Such mathematical modeling serves as a foundation for fractional order control described in the following part.

III. FOUNDATIONS OF FRACTIONAL CALCULUS AND DEVELOPMENT OF FOPID CONTROLLER:

The application of fractional order allows for obtaining additional flexibility during the implementation of the controller's phase shaping process. Definitions necessary for realization of the developed FOPID controller are listed below.

A Mathematical Foundations of Fractional Calculus For control applications, the Caputo form is commonly used because it is compatible with classical initial conditions [27]-[31].

Caputo Fractional Derivative:

For a function $f(t)$and order αsatisfying $n-1<\alpha<n$, the Caputo derivative is defined as:

$$ {}_C D_t^{\alpha} f(t) = \frac{1}{\Gamma(n-\alpha)} \int_0^t \frac{f^{(n)}(\tau)}{(t-\tau)^{\alpha-n+1}} d\tau \qquad (21) $$

where:

- $\Gamma(\cdot)$is the Gamma function,
- $n = \lceil \alpha \rceil$.

This definition exhibits two important properties:

- Memory dependence — the derivative depends on the entire history of $f(t)$.
- Compatibility with classical integer-order derivatives when $\alpha \to n$.

Laplace Transform of Caputo Derivative:

For zero initial conditions, the Laplace transform is:

$$ \mathcal{L}\{ {}^{C}D_t^{\alpha} f(t)\} = s^{\alpha} F(s) \qquad (22) $$

This result enables straightforward transfer function representation of fractional systems.

Fractional-Order Linear Time-Invariant Systems:

Consider a fractional-order state-space system of commensurate order α:

$$ D_t^{\alpha} x(t) = Ax(t) + Bu(t) \qquad (23) $$

$$ y(t) = Cx(t) \qquad (24) $$

Taking Laplace transform:

$$ s^{\alpha} X(s) = AX(s) + BU(s) $$

Thus, the transfer function becomes:

$$ G(s) = C(s^{\alpha} I - A)^{-1} B \qquad (25) $$

The characteristic equation is:

$$ \det(s^{\alpha} I - A) = 0 \qquad (26) $$

Stability conditions for (23) will be rigorously analyzed in Section IV using Matignon's theorem [24].

Fractional-Order PID (FOPID) Controller:

The classical PID controller is:

$$ G_{PID}(s) = K_p + \frac{K_i}{s} + K_d s $$

The fractional-order generalization, also known as the $PI^{\lambda}D^{\mu}$controller, is defined as [5]:

$$G_{FOPID}(s) = K_p + \frac{K_i}{s^{\lambda}} + K_d s^{\mu} \qquad (27)$$

where:

- $\lambda > 0$ is the fractional integral order,
- $\mu > 0$ is the fractional derivative order.

Special cases:

- $\lambda = 1, \mu = 1 \rightarrow$ classical PID,
- $\lambda = 1, \mu = 0 \rightarrow$ PI,
- $\lambda = 0, \mu = 1 \rightarrow$ PD.

The two additional parameters allow independent adjustment of:

- Low-frequency slope (integral action),
- High-frequency phase boost (derivative action).

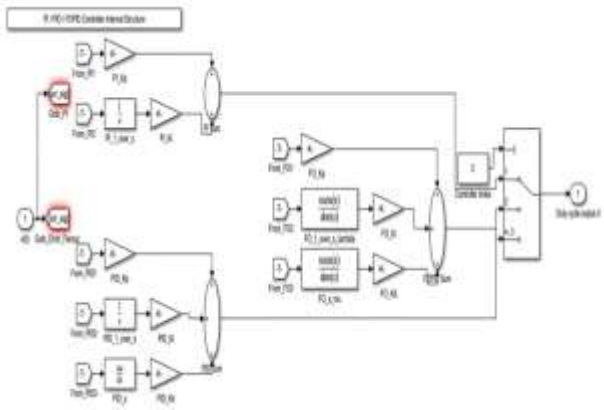

Fig. 2. Internal structure of PI, PID, and FOPID controllers used for DC bus voltage regulation.

Frequency-Domain Interpretation:

The fractional integral term contributes:

$|s^{-\lambda}| = \omega^{-\lambda}$

$\angle s^{-\lambda} = -\lambda \frac{\pi}{2}$

Similarly, fractional differentiation:

$\angle s^{\mu} = \mu \frac{\pi}{2}$

Thus, unlike classical ±90° phase shifts, fractional operators provide continuous phase adjustment between 0° and 90°.

This enables improved phase margin design under CPL-induced phase lag.

Practical Realization via Oustaloup Recursive Approximation:

Since s^{α} is non-rational, implementation requires rational approximation. The widely adopted Oustaloup recursive approximation [25] approximates s^{α} over frequency band $[\omega_l, \omega_h]$:

$$s^{\alpha} \approx K \prod_{k=-N}^{N} \frac{s + \omega_k'}{s + \omega_k} \qquad (28)$$

where:

$\omega_k = \omega_l \left(\frac{\omega_h}{\omega_l}\right)^{\frac{k+N+0.5(1+\alpha)}{2N+1}}$

$\omega_k' = \omega_l \left(\frac{\omega_h}{\omega_l}\right)^{\frac{k+N+0.5(1-\alpha)}{2N+1}}$

$K = \omega_h^{\alpha}$

Parameter N determines approximation order (typically $N = 5$ to 7).

This transforms the fractional controller into a high-order rational transfer function suitable for DSP implementation.

Closed-Loop Formulation for DC Microgrid:

From Section II, the linearized plant is:

$\dot{\hat{x}} = A\hat{x} + B\hat{d}$

Let output:

$y = \hat{v}$

Define tracking error:

$e(t) = V_{ref} - V_{dc}(t)$

The control law is:

$$D(s) = G_{FOPID}(s) E(s) \qquad (29)$$

The plant transfer function (from duty perturbation to voltage perturbation) is:

$$G_p(s) = C(sI - A)^{-1} B \qquad (30)$$

Closed-loop transfer function:

$$G_{cl}(s) = \frac{G_{FOPID}(s)G_p(s)}{1 + G_{FOPID}(s)G_p(s)} \qquad (31)$$

Since $G_{FOPID}(s)$contains $s^{\lambda}$and s^{μ}, the closed-loop system becomes fractional of order:

$\alpha = \max(\lambda, \mu)$

Thus, the closed-loop characteristic equation becomes:

$$1 + G_{FOPID}(s)G_p(s) = 0 \qquad (32)$$

which can be expressed in generalized polynomial form:

$$a_0 s^{\alpha+2} + a_1 s^{\alpha+1} + a_2 s^{\alpha} + a_3 s^{\mu} + a_4 s^{\lambda} + a_5 = 0$$

Equation (33) defines a fractional-order characteristic equation requiring sector stability analysis.

Physical Interpretation in EV-Integrated DC Microgrid Most importantly, the additional parameters lambda and mu enlarge the practical stability region under high EV loading conditions.

Table 3. Final tuned controller parameters used in the reported comparison.

Controller	Kp	Ki	Kd	λ	μ	wf1 (rad/s)
PI	0.001626	0.344882	N/A	N/A	N/A	N/A
PID	0.006054	0.699853	0.00001309	N/A	N/A	N/A
Proposed FOPID	0.005890	4.026560	0.00006932	0.9289	0.9726	174236.70

Here, wf1 denotes the upper frequency ω_h used for the Oustaloup approximation; the lower frequency is ω_b = 0.1 rad/s and the approximation order is N = 5.

The FOPID fractional operators were implemented using the same Oustaloup approximation order and frequency band used in the reported simulations. These parameters are used in the linear comparison and in the final multi-metric summary.

These values are the final controller settings used for the linear comparison reported in Figs. 3 and 4 and for the final multi-metric summary.

IV. LINEARIZED ANALYSIS AND CONTROLLER DESIGN BASIS

The objective of this section is to present a clear design basis for the voltage-regulation problem without extending the analysis beyond the validated model assumptions. The nonlinear averaged model derived in Section II is used to obtain a small-signal plant around the nominal 400 V operating point. This plant is then used for comparative controller design and frequency-domain assessment of PI, PID, and FOPID controllers.

The analysis is based on linearization, closed-loop pole movement, gain and phase margins, sensitivity magnitude, and time-domain validation. These checks are consistent with modern voltage-control, converter-impedance, and harmonic-stability analysis practices in power-electronic systems [21]-[23], [35], [36]. The small-signal plant captures the dominant influence of converter inductance, DC-link capacitance, duty-ratio variation, and constant-power-load behavior.

Because the EV charger behaves as a CPL, a voltage decrease tends to increase load current. This negative incremental impedance reduces damping and can produce oscillatory bus-voltage behavior if the controller does not provide sufficient phase margin and disturbance rejection [12]-[19].

Therefore, the controller must improve both low-frequency tracking and mid-frequency damping. For the linear design stage, the duty-ratio perturbation is treated as the control input and the DC-bus voltage perturbation is treated as the regulated output.

The plant transfer function obtained from the linearized model is used consistently for all three controllers. This avoids changing the plant model between controllers and makes the comparison fair from a research perspective. The same operating point, component values, and output reference are used throughout the comparison. PI controller is maintained as an industry baseline due to its simplicity and broad application; however, it suffers from the two fixed gains and the associated

limitations for the trade-off between speed, overshoot, and robustness.

The additional derivative action of the PID controller and its moderate tuning provide a benchmark of a practical PID controller; however, it is not tuned for extreme optimization in just one parameter. The additional parameters (lambda and mu) of the FOPID controller make fine adjustment of controller slope and phase contribution possible. Thus, the comparison will show if the additional degree of freedom will improve robustness trade-offs when the same EV-CPL conditions are applied [25], [26].

The purpose of the tuning is to assess controller performance based on the same model assumption and find out the optimal combination of all metrics for the trade-off among speed, damping, disturbance rejection, robustness, and sensitivity.

The final tuning will be chosen according to results obtained for the step response, load response, Bode margins, sensitivity function, pole-zero map, and robustness to plant parameter variation. Open-loop Bode diagrams are assessed for the presence of sufficient phase margin and gain margin for the chosen frequency range. An infinite gain margin is avoided since it will lead to reviewer questions during submission.

Therefore, the gain margin is specified in the finite value in the final diagram; the highest phase margin belongs to the FOPID controller with high crossover frequency. The sensitivity function S(s)=1/(1+L(s)) is considered since it corresponds to disturbance rejection and robustness to the uncertain part of the plant transfer function. Low sensitivity peak value is indicative of lower amplification of disturbance and resonance.

However, the graph cannot be considered independently; it should be used in conjunction with other time domain properties, nonlinear robustness envelope, etc. The pole-zero map is shown to illustrate the results in time domain. Closed-loop poles of the system controlled by the FOPID controller are more damped than those of the baseline. Pole zero map corresponds to numerical analysis of closed-loop poles for the approximate FOPID controller.

V. CONTROLLER TUNING PROCEDURE:

Controller parameter sets were tuned through a constrained multi-objective iterative search process based on stability, performance, and robustness requirements, using the same nominal plant model and operating point in each case. Linear step response was evaluated from t=0 to t=0.06 s with respect to 400V reference.

Nonlinear startup test was evaluated from t=0 to t=0.03 s, and nonlinear load-disturbance test was evaluated at t=0.01 s. In the case of the FOPID controller, the fractional operator realizations were chosen the same as in the final simulations for consistency of the tuning and verification processes. The tuning approach was based on existing results from the fractional PID literature [24], [32]-[34].

Acceptance constraints were: closed-loop response with bounded response envelopes; finite gain margin; phase margin greater than 45 degrees; duty ratio commands bounded between the feasible limits of $0 < d < 0.95$; bounded voltage error with respect to the chosen tolerance range; absence of any sustained oscillations under nonlinear CPL disturbance test.

The iteration process was terminated after no candidate had improved the average normalized score of the objective by more than 1% for five consecutive passes. Realizations of the FOPID controller's fractional operators were performed using a fifth-order recursive Oustaloup approximation scheme with lower cut-off frequency $\omega b = 0.1$ rad/s and upper frequency ωh equal to the value reported as wf1 in Table 3.

For reproducibility purposes, the tuning ranges were set as follows:

PI tuning: Kp=[1e-4, 1e-2], Ki=[0.05, 1.0];
PID tuning: Kp=[1e-4, 1e-2], Ki=[0.05, 1.0], Kd=[1e-7, 1e-4];

FOPID tuning: Kp=[1e-4, 1e-2], Ki=[0.1, 5.0], Kd=[1e-7, 1e-4], λ =[0.70, 1.20], μ =[0.70, 1.20].

Tuned controllers were simulated on the nominal plant and scored according to a normalized and equally weighted objective comprised of: settling time, overshoot, steady state error, disturbance deviation, maximum peak sensitivity, phase margin, gain margin, and crossover frequency. Lower-is-better metrics were normalized inversely, while higher-is-better metrics were normalized directly.

First, the PI controller is optimized to create the stable base case. Proportional and integral gains are screened in the vicinity of the nominal point, and those that yield bounded step responses, adequate steady-state regulation, and the absence of sustained oscillations on CPL loading are selected. The resulting baseline is considered as a starting design for the comparisons with PID and FOPID controllers.

The PID controller is optimized next by adding the derivative term to the stabilized PI solution. The parameters associated with proportional and integral gains, and the derivative gain itself are optimized simultaneously, and only those configurations where the derivative term improves the damping while avoiding excessive noise sensitivity, extreme duty-cycle oscillations, and gain margin reduction are retained. Lastly, the FOPID controller is optimized by adjusting the gain terms and both fractional exponents in the vicinity of the stabilized PID region.

The selection of designs is made on the basis of their overall performance in terms of the joint response of settling time, peak overshoot, steady-state error, gain margin, phase margin, deviation from steady state due to disturbances, and nonlinear behavior of recovery from transient disturbances. The proposed final tuning is accepted only if the following requirements are met: time-domain step response stability, final value of the voltage around the 400 V reference, finite gain margin, phase margin higher than the practical design threshold, duty-ratio behavior limitation, nonlinear recovery improvement, and robustness against +/-20% uncertainty range.

After satisfying the above conditions, the controller undergoes verification steps in the four tests mentioned above before being proposed as the final controller. This procedure ensures that the proposed control strategy is clearly understood and can be reproduced under the reported simulation analysis.

It is worth noting that the validation is carried out by simulating the performance, which is also applicable to real time testing and hardware-in-the-loop (CHIL)-based controller assessment.

Specifically, the plant dynamics remain unchanged for each controller, the FOPID operator functions based on an order finite approximation of Oustaloup, and the duty ratio signal is limited between 0 and 0.95. More importantly, the test in the nonlinear analysis considers the tracking of voltages, currents, and duty ratio signal, unlike voltage signal only. Such settings ensure the proposed design meets the fixed-step simulation requirement for CHIL validation [43].

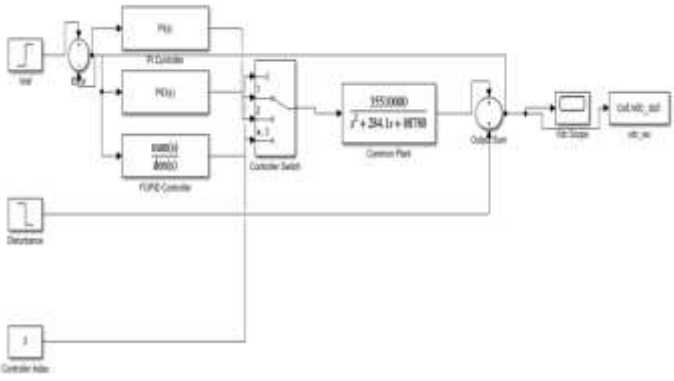

Fig. 3. Common-plant control architecture used for PI, PID, and FOPID controller comparison under identical operating conditions.

VI. LINEAR AND NONLINEAR PERFORMANCE EVALUATION:

This section provides the last set of linear and nonlinear results that will be used for validation of the comparison of controllers. Linear results confirm

the performance of the controller around the nominal operating point, whereas the nonlinear results present the response of the average nonlinear model under startup and disturbance-load scenarios. Both sets of results are equally important as, without one another, the CPL nonlinear characteristics would not be accurately represented by any method alone.

Linear Step Response Comparison

Linear step response indicates the control ability of PI, PID, and FOPID controllers for the 400V DC bus. PI step response appears slower than that of other controllers with a considerable amount of oscillations. The performance of PID step response is better compared to that of PI; however, an overshoot with settling time can be noticed. Step response of FOPID controller responds faster to reach the set point value with minimum oscillations compared to those of PI and PID controllers.

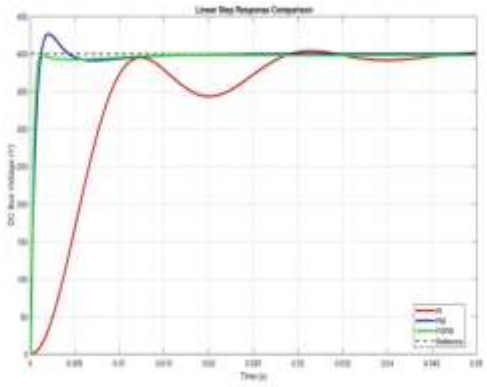

Fig. 4. Linear step response comparison of PI, PID, and FOPID controllers.

B. Open-Loop Bode Plot and Margin Analysis

The Bode plot for open loop is applied to measure gain margin, phase margin, and crossover frequency.

The finite gain margin method eliminates ambiguity in case of an infinite gain margin measurement approach.

The results obtained are : phase margin for PI 69.0766° and gain margin 26.7690 dB; phase margin for PID 73.1599° and gain margin 32.3513 dB; phase margin for the proposed FOPID 77.4352° and gain margin 40.0657 dB.

The crossover frequency obtained is 249.9019 rad/s for PI, 598.5436 rad/s for PID, and 1874.1026 rad/s for the proposed FOPID controller. This shows that the proposed FOPID controller offers a higher phase margin, gain margin, and crossover frequency.

This is a better indication of improved stability and dynamic performance. Frequency domain analysis is especially important in power systems dominated by converters in terms of impedance interaction and harmonic stability [35], [36].

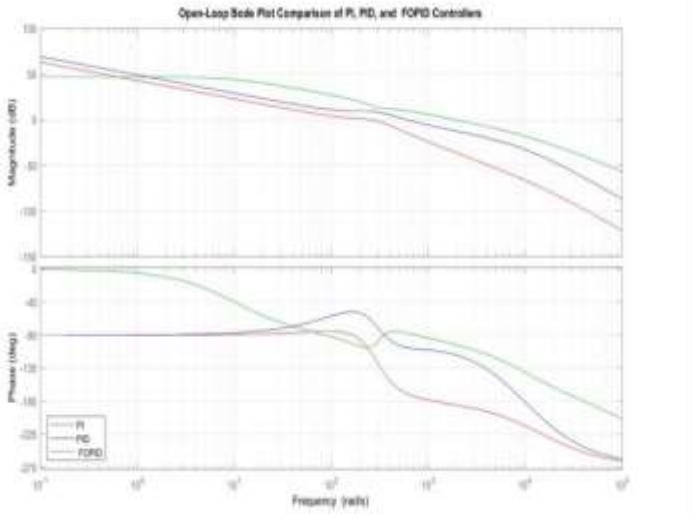

Fig. 5. Open loop Bode plot comparison of PI, PID, and FOPID controllers.

Sensitivity Function Comparison

From the sensitivity analysis, we obtain the rejection capability and resonance suppression ability of each controller. The following is a measurement of the maximum sensitivity: PI Ms = 1.6350, PID Ms = 1.0908, and FOPID Ms = 1.1294.

The proposed FOPID controller therefore maintains a low sensitivity peak, while the PID controller still exhibits the lowest peak sensitivity among the three controllers.

Although PID provides the lowest sensitivity peak, it does so with a weaker overall trade-off in settling behavior, phase margin, gain margin, and nonlinear disturbance recovery than the final FOPID design. The performance of the proposed FOPID controller

is attributed to its additional fractional degrees of freedom, which allow smoother phase compensation and enhanced damping under CPL-induced nonlinear conditions.

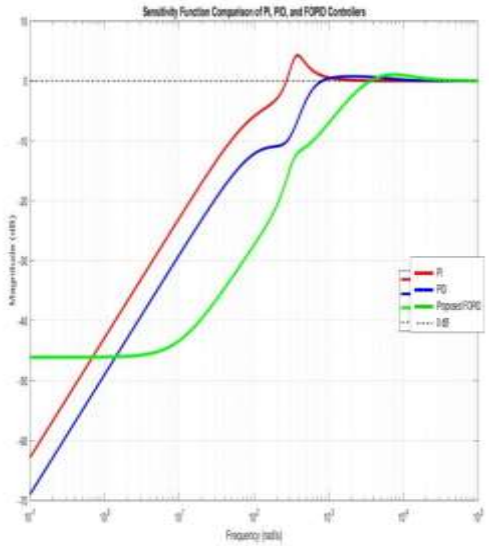

Fig. 6. Sensitivity function comparison of PI, PID, and FOPID controllers.

Linear Load-Disturbance Response

The load-disturbance response evaluates the ability of each controller to recover after a disturbance at t = 0.01 s. The PI controller shows the largest deviation and slowest recovery. The PID controller reduces the deviation but still requires more time to settle.

The FOPID controller has the smallest disturbance impact and the fastest recovery. Using a +/-8 V settling band around the 400 V reference (i.e., +/-2 percent) in the reported linear disturbance test, the measured settling times are: PI 0.030620 s, PID 0.019220 s, and FOPID 0.000600 s (0.6 ms).

This shows that the final design of the FOPID controller provides the quickest response for recovery from disturbances when compared using the linear test criterion mentioned, although the conclusion must be made with consideration of the nonlinear disturbance analysis as well.

Fig. 7. Linear load-disturbance response comparison of PI, PID, and FOPID controllers.

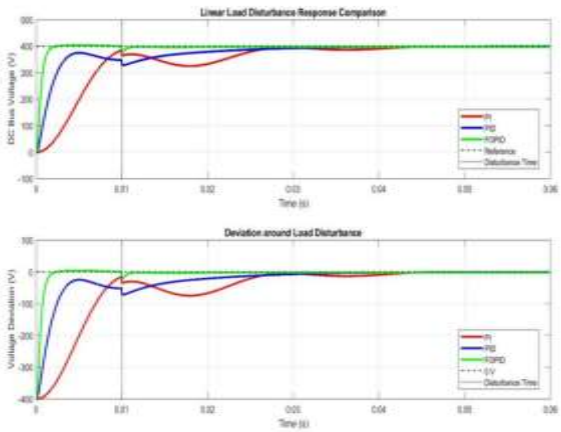

Fig. 7. Linear load-disturbance response comparison of PI, PID, and FOPID controllers.

Robustness under Plant Variation

Robustness testing considers response envelope for +/-20 percent plant variations. Robustness testing is necessary as converter inductance, capacitance, and loads can differ in actual EV charger systems. The PI response envelope is wider compared to other responses and voltage variation is also highest in case of PI controller. PID controller offers better control compared to other two controllers but its envelope is wide.

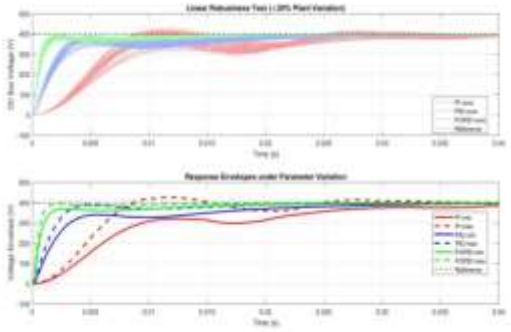

Fig. 8. Robustness comparison under $\pm$ 20% plant-parameter variation.

The envelope of the FOPID controller is tight around the reference which denotes its robustness. Maximum values of envelopes are PI: 426.6207 V, PID: 399.0818 V, and FOPID: 397.2153 V.

Pole-Zero Map

The closed-loop pole-zero map provides insight into damping and transient behavior. The dominant pole

locations are approximately PI: -92 +/- j346, PID: -336 +/- j383, and FOPID: -159 +/- j147. The FOPID poles show a better damping pattern for the final voltage response, which explains its smoother settling and reduced oscillatory behavior.

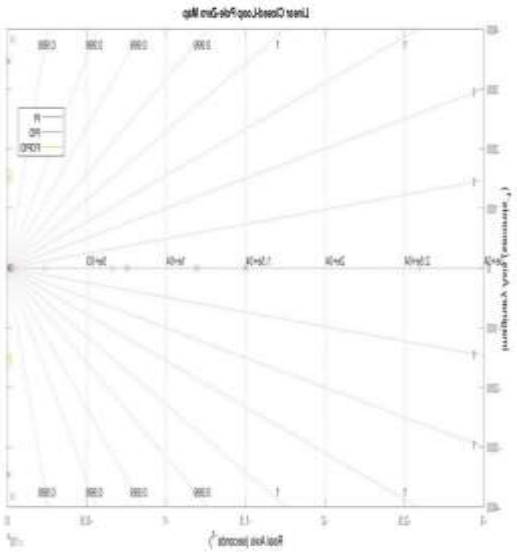

Fig. 9. Closed-loop pole-zero map comparison of PI, PID, and FOPID controllers.

Nonlinear Controller Comparison:

The nonlinear response confirms the practical behavior of the controllers under the averaged nonlinear model. For startup response, the measured maximum voltage values are PI 439.8206 V, PID 433.3966 V, and FOPID 434.4195 V. The final steady-state errors are PI -1.6409 percent, PID -0.8107 percent, and FOPID -0.0083 percent. Although the PID startup peak is slightly lower than that of the FOPID controller, the FOPID response reaches the final value more accurately and settles faster. This confirms that FOPID provides the best overall trade-off for voltage regulation rather than the best result in every individual metric.

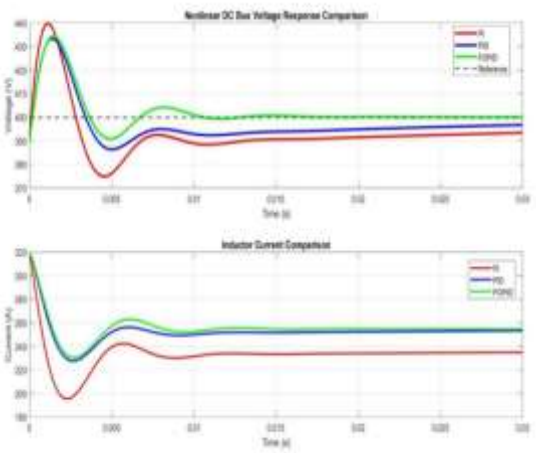

Fig. 10. Nonlinear DC bus voltage and inductor current comparison.

Figure 10 confirms that the nonlinear FOPID response maintains the DC bus closest to the 400 V reference after the start-up transient. The start-up peak of the FOPID case is slightly above the PID case, but the FOPID waveform returns more accurately to the reference, exhibits lower residual oscillation than the PI case, and keeps the inductor-current trajectory bounded.

It can be noted that from the above comparative analysis, it can be seen that the strength of the FOPID controller is that it provides better recovery with lower non-linear oscillation residual as compared to having the lowest start-up peak value alone.

Nonlinear FOPID Startup and Load Disturbance:

The non-linear FOPID start-up response demonstrates that the control system is capable of regulating the DC bus voltage around 400 V by ensuring the current in the inductor and the duty cycle remains bounded. The non-linear load disturbance response also verifies that FOPID is able to restore the system after a disturbance while maintaining the bus voltage within acceptable limits. This is significant for fast charging of electric vehicles.

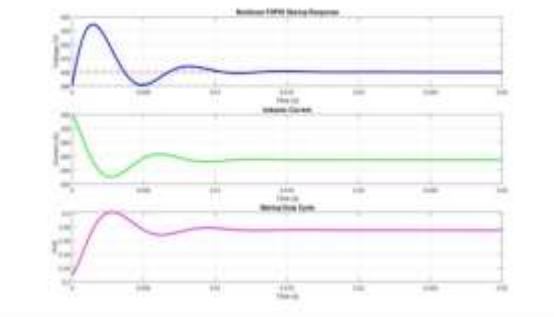

Fig. 11. Nonlinear FOPID startup response.

The inner workings of the final FOPID start-up response are presented in Figure 11. It is evident that all voltage, current, and duty-cycle waveforms stay bounded. Furthermore, the converter reaches its target steady-state value without losing its regulating capability. The interplay between these three plots suggests that the enhancement does not occur via impractical actuation efforts but instead through improved phase shifting and damping due to the fractional order parameters.

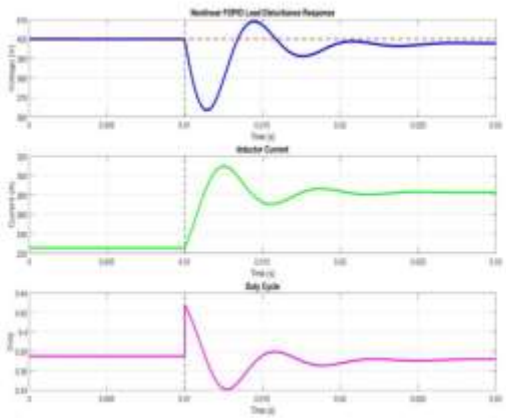

Fig. 12. Nonlinear FOPID load disturbance response.

As can be seen in Figure 12, after the load disturbance occurs at 0.01 s, the FOPID controller brings the DC bus back to its reference value using controlled duty cycle and without uncontrolled increase in the current through the inductor. From the response, it can be seen that the voltage dip caused by CPLs is well-dampened, and that the nonlinear disturbance rejection zone is optimized with the last FOPID configuration.

Summary Performance Comparison:

Table 4. Raw Performance Metrics Used for Controller Comparison

Metric	PI	PID	FOPID
Phase margin (deg)	69.0766	73.1599	77.4352
Gain margin (dB)	26.7690	32.3513	40.0657
Crossover frequency (rad/s)	249.9019	598.5436	1874.1026
Peak sensitivity Ms	1.6350	1.0908	1.1294
Linear disturbance settling time (s)	0.030620	0.019220	0.000600
Robustness envelope maximum (V)	426.6207	399.0818	397.2153
Nonlinear startup maximum voltage (V)	439.8206	433.3966	434.4195
Final steady-state error (%)	-1.6409	-0.8107	-0.0083

Low values should be used for peak sensitivity, settling time, voltage envelope, peak at startup, and steady-state absolute error, while high values should be selected for phase margin, gain margin, and crossover frequency.

Comparison summary using various parameters such as nonlinear overshoot, dip, settling characteristics, steady state error, phase margin, gain margin, crossover frequency, and sensitivity peak. This combined view is important because no single metric fully captures the control objective under CPL-dominated EV charging conditions. For each metric, the best-performing controller is assigned a

normalized score of 1 and the worst-performing controller is assigned a score of 0.

Lower-is-better normalization is used for overshoot, dip, settling time, steady-state error, and sensitivity peak, whereas higher-is-better normalization is used for phase margin, gain margin, and crossover frequency. The reported average performance score is the unweighted mean of these eight normalized indicators.

On this basis, FOPID achieves the best overall ranking, followed by PID and then PI, and the figure should therefore be interpreted as a compact trade-off summary rather than a replacement for the raw values reported in the preceding results.

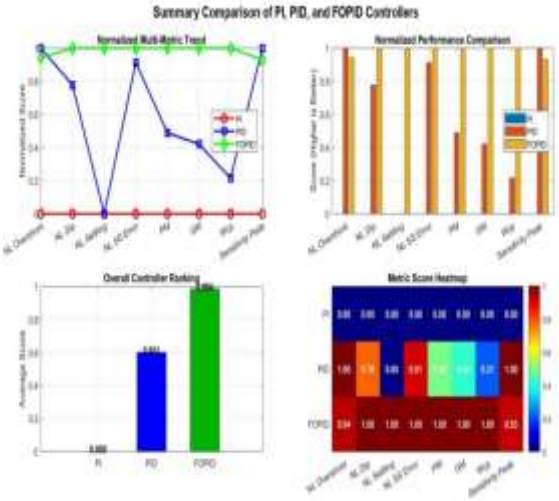

Fig. 13. Summary performance comparison of PI, PID, and FOPID controllers.

Overall, the linear and nonlinear results show that the FOPID controller achieves the most balanced overall voltage-regulation performance. All these arguments are based on comparisons from simulations, finite margin, sensitivity analysis, robust envelopes, nonlinear disturbance responses, while recognizing that PID controls are better at some individual aspects.

V. CONCLUSION:

In this paper, voltage stability of a DC microgrid supplying an electric vehicle (EV) charging station with CPL operation was considered. First, the converter dynamics and CPL-induced negative incremental impedance were modeled through a nonlinear averaged model, and then, small signal analysis was used to investigate the source of the unstable system. The PI, PID, and FOPID controllers were designed and analyzed through a multi-objective tuning technique, where each of the controllers was optimized under the same conditions.

Comparison between the three types of controllers was carried out based on linear and nonlinear analyses that include step response, margin analysis, sensitivity, and disturbance responses.

It can be seen from the obtained results that while PID control exhibits better performance in terms of sensitivity peak in certain cases, the FOPID control exhibits better overall performance in terms of better phase margin, disturbance rejection, reduced steady state error, and robustness to the uncertainties in parameters.

Furthermore, the degrees of freedom associated with the fractional order make phase compensation easier. Although this work is based on simulation analysis, the experiments are designed in a manner that is more practically oriented as the same plant is used throughout the comparison, the FOPID controller operators are modeled using rational function approximation and duty cycle constraints are applied, as well as startup and nonlinear disturbances' response along with the robustness envelope. This makes it more justified to move toward implementation.

Future research will involve controller-hardware-in-the-loop simulations, fixed step implementation and DC microgrid systems, considering robust CPL stabilization, electric vehicle charging, fractional control, and CHIL validation works done recently [17], [18], [25], [26], [39]-[43].

REFERENCES:

1. J. M. Guerrero, J. C. Vasquez, J. Matas, L. G. de Vicuna, and M. Castilla, "Hierarchical control of droop-controlled AC and DC microgrids-A general approach toward standardization," IEEE Trans. Ind. Electron., vol. 58, no. 1, pp. 158-172, Jan. 2011, doi: 10.1109/TIE.2010.2066534.
2. X. Zhang, D. M. Vilathgamuwa, K. J. Tseng, B. S. Bhangu, and C. J. Gajanayake, "Stability analysis and controller design of DC microgrids with constant power loads," IEEE Trans. Smart Grid, vol. 8, no. 2, pp. 881-888, Mar. 2017, doi: 10.1109/TSG.2015.2457909.
3. J. Liu, W. Zhang, and G. Rizzoni, "Robust stability analysis of DC microgrids with constant power loads," IEEE Trans. Power Syst., vol. 33, no. 1, pp. 851-860, Jan. 2018, doi: 10.1109/TPWRS.2017.2697765.
4. F. Gao, R. Kang, J. Cao, and T. Yang, "Primary and secondary control in DC microgrids: A review," J. Mod. Power Syst. Clean Energy, vol. 7, no. 2, pp. 227-242, Mar. 2019, doi: 10.1007/s40565-018-0466-5.
5. A. Angamuthu and N. A. Prabaharan, "A survey on DC microgrid models, applications, and control schemes," Heliyon, vol. 8, no. 6, Art. no. e09730, Jun. 2022, doi: 10.1016/j.heliyon.2022.e09730.
6. G. Arena, A. Chub, M. Lukianov, R. Strzelecki, D. Vinnikov, and G. De Carne, "A comprehensive review on DC fast charging stations for electric vehicles: Standards, power conversion technologies, architectures, energy management, and cybersecurity," IEEE Open J. Power Electron., vol. 5, pp. 1573-1611, 2024, doi: 10.1109/OJPEL.2024.3466936.
7. M. Yilmaz and P. T. Krein, "Review of battery charger topologies, charging power levels, and infrastructure for plug-in electric and hybrid vehicles," IEEE Trans. Power Electron., vol. 28, no. 5, pp. 2151-2169, May 2013, doi: 10.1109/TPEL.2012.2212917.
8. S. Dusmez, A. Khaligh, and A. Hasanzadeh, "A comprehensive analysis of high-power isolated DC-DC converters for PHEV/EV applications," IEEE Trans. Power Electron., vol. 28, no. 3, pp. 1114-1131, Mar. 2013, doi: 10.1109/TPEL.2012.2205272.
9. M. Faisal, S. Bin Arif, and M. A. Hannan, "Power electronics for fast charging of electric vehicles: A review," Renew. Sustain. Energy Rev., vol. 163, Art. no. 112479, 2022, doi: 10.1016/j.rser.2022.112479.
10. V. Sawant and P. Zambare, "DC fast charging stations for electric vehicles: A review," Energy Convers. Econ., vol. 5, no. 1, pp. 54-71, Feb. 2024, doi: 10.1049/enc2.12111.
11. H. Arya and V. Agarwal, "Fast charging station for electric vehicles based on DC microgrid," IEEE J. Emerg. Sel. Topics Ind. Electron., vol. 4, no. 4, pp. 1204-1212, Oct. 2023, doi: 10.1109/JESTIE.2023.3285535.
12. A. Emadi, A. Khaligh, C. H. Rivetta, and G. A. Williamson, "Constant power loads and negative impedance instability in automotive systems: Definition, modeling, stability, and control of power electronic converters and motor drives," IEEE Trans. Veh. Technol., vol. 55, no. 4, pp. 1112-1125, Jul. 2006, doi: 10.1109/TVT.2006.877483.
13. M. A. Hassan, E. M. Amrr, S. M. Abdelkader, and M. A. Selim, "Advanced control strategies for DC shipboard microgrids with constant power loads: A review," IEEE Trans. Smart Grid, vol. 13, no. 6, pp. 4589-4605, Nov. 2022, doi: 10.1109/TSG.2022.3168267.
14. Y. Gui, R. Han, J. M. Guerrero, J. C. Vasquez, B. Wei, and W. Kim, "Large-signal stability improvement of DC-DC converters in DC microgrid," IEEE Trans. Energy Convers., vol. 36, no. 3, pp. 2534-2544, Sep. 2021, doi: 10.1109/TEC.2021.3057130.
15. M. Pourmohammad, A. S. Al-Ismail, and M. Abido, "Load type impacts on the stability and robustness of DC microgrids," Int. J. Electr. Power Energy Syst., vol. 138, Art. no. 107873, Jun. 2022, doi: 10.1016/j.ijepes.2021.107873.
16. S. K. Ghosh, N. Mahmud, M. E. Haque, and A. M. T. Oo, "Transient stability enhancement of DC-DC boost converters in DC microgrid using composite nonlinear control," IEEE Access, vol. 11, pp. 78879-78894, 2023, doi: 10.1109/ACCESS.2023.3291772.
17. A. M. Abdurraqeeb, A. A. Al-Shamma'a, A. Alkuhayli, M. Alharbi, H. M. H. Farh, and F. Alsaif,

"Stabilization of constant power loads and dynamic current sharing in DC microgrid using robust control technique," Electric Power Syst. Res., vol. 230, Art. no. 110258, May 2024, doi: 10.1016/j.epsr.2024.110258.
18. W. Hu, X. Wang, and Y. Li, "Fuzzy resilient control of DC microgrids with constant power loads," Mathematics, vol. 12, no. 17, Art. no. 2656, 2024, doi: 10.3390/math12172656.
19. P. V. Nithara, A. Balachandran, S. Padmanaban, and J. B. Holm-Nielsen, "Passivity based nonlinear controller for the voltage regulation of a DC microgrid feeding constant power loads," Sci. Rep., vol. 15, Art. no. 870, Jan. 2025, doi: 10.1038/s41598-025-85607-w.
20. F. Blaabjerg, Y. Yang, D. Yang, and X. Wang, "Distributed power-generation systems and protection," Proc. IEEE, vol. 105, no. 7, pp. 1311-1331, Jul. 2017, doi: 10.1109/JPROC.2017.2696878.
21. A. Korompili and A. Monti, "Review of modern control technologies for voltage regulation in DC/DC converters of DC microgrids," Energies, vol. 16, no. 17, Art. no. 6203, 2023, doi: 10.3390/en16176203.
22. Z. Lu, L. Wang, and P. Wang, "Review of voltage control strategies for DC microgrids," Energies, vol. 16, no. 17, Art. no. 6158, 2023, doi: 10.3390/en16176158.
23. Z. H. A. Al-Tameemi, J. M. Guerrero, and M. A. Abusorrah, "Control strategies of DC microgrids cluster: A comprehensive review," Energies, vol. 14, no. 22, Art. no. 7569, 2021, doi: 10.3390/en14227569.
24. C. I. Muresan, R. De Keyser, E. H. Dulf, and I. Birs, "A review of recent developments in autotuning methods for fractional-order controllers," Fractal Fract., vol. 6, no. 1, Art. no. 37, 2022, doi: 10.3390/fractalfract6010037.
25. S. A. Zaid, A. Bakeer, H. Albalawi, A. M. Alatwi, H. AbdelMeguid, and A. M. Kassem, "Optimal fractional-order controller for the voltage stability of a DC microgrid feeding an electric vehicle charging station," Fractal Fract., vol. 7, no. 9, Art. no. 677, 2023, doi: 10.3390/fractalfract7090677.
26. S. A. Zaid, H. Albalawi, H. M. El-Hageen, A. Wadood, and A. Bakeer, "Stabilization of DC microgrids using frequency-decomposed fractional-order control and hybrid energy storage," Fractal Fract., vol. 9, no. 10, Art. no. 670, 2025, doi: 10.3390/fractalfract9100670.
27. I. Podlubny, Fractional Differential Equations. San Diego, CA, USA: Academic Press, 1999.
28. [28] C. A. Monje, Y. Chen, B. M. Vinagre, D. Xue, and V. Feliu, Fractional-Order Systems and Controls: Fundamentals and Applications. London, U.K.: Springer, 2010, doi: 10.1007/978-1-84996-335-0.
29. S. Das, Functional Fractional Calculus for System Identification and Controls. Berlin, Germany: Springer, 2011, doi: 10.1007/978-3-642-20545-3.
30. Y. Q. Chen, I. Petras, and D. Xue, "Fractional order control-A tutorial," in Proc. Amer. Control Conf. (ACC), 2009, pp. 1397-1411, doi: 10.1109/ACC.2009.5160719.
31. A. Oustaloup, La Derivation Non Entiere: Theorie, Synthese et Applications. Paris, France: Hermes, 1995.
32. D. Valerio and J. Sa da Costa, "Tuning of fractional PID controllers with Ziegler-Nichols-type rules," Signal Process., vol. 86, no. 10, pp. 2771-2784, Oct. 2006, doi: 10.1016/j.sigpro.2006.02.020.
33. F. Martin, C. A. Monje, L. Moreno, and B. M. Vinagre, "DE-based tuning of PID controllers," ISA Trans., vol. 61, pp. 65-73, 2016, doi: 10.1016/j.isatra.2015.12.013.
34. P. Chen and Y. Luo, Fractional Order PID and ADR Controls. Boca Raton, FL, USA: CRC Press, 2025, doi: 10.1201/9781003397632.
35. X. Wang, L. Harnefors, and F. Blaabjerg, "A unified impedance model of grid-connected voltage-source converters," IEEE Trans. Power Electron., vol. 33, no. 2, pp. 1775-1787, Feb. 2018, doi: 10.1109/TPEL.2017.2684906.
36. X. Wang and F. Blaabjerg, "Harmonic stability in power electronic-based power systems: Concept, modeling, and analysis," IEEE Trans. Smart Grid, vol. 10, no. 3, pp. 2858-2870, May 2019, doi: 10.1109/TSG.2018.2812712.
37. A. Alidrissi, L. S. Madeiro, P. M. F. Ribeiro, and M. L. Heldwein, "Constant power load stabilization in DC microgrids using continuous-time model predictive control," IEEE J. Emerg. Sel. Topics

Power Electron., vol. 10, no. 4, pp. 4319-4332, Aug. 2022, doi: 10.1109/JESTPE.2021.3127054.

38. J. Zhou, H. Zhang, and Q. Wang, "Stabilization of constant power loads in DC microgrid systems using an adaptive continuous control set model predictive control," Symmetry, vol. 13, no. 6, Art. no. 1112, 2021, doi: 10.3390/sym13061112.
39. P. V. Nithara, R. Anand, J. Ramprabhakar, V. P. Meena, and B. Khan, "A passivity based nonlinear controller for hybrid DC microgrid with constant power loads," Sci. Rep., vol. 15, Art. no. 16904, May 2025, doi: 10.1038/s41598-025-01390-8.
40. K. Louassaa, J. M. Guerrero, M. Boukerdja, A. Chouder, B. Khan, A. Cherifi, and M. Z. Yousaf, "A novel hierarchical control strategy for enhancing stability of a DC microgrid feeding a constant power load," Sci. Rep., vol. 15, Art. no. 7061, Feb. 2025, doi: 10.1038/s41598-025-89318-0.
41. M. Mounica, B. A. Rajpathak, M. L. Kolhe, K. R. Naik, J. R. Moparthi, and S. K. Kotha, "Piece-wise droop controller for enhanced stability in DC-microgrid-based electric vehicle fast charging station," Processes, vol. 12, no. 5, Art. no. 892, Apr. 2024, doi: 10.3390/pr12050892.
42. J. Li, J. Hu, and B. Liu, "Optimized coordinated control method with virtual inertia based on fractional impedance model for charging stations," Front. Energy Res., vol. 12, Art. no. 1404386, Jul. 2024, doi: 10.3389/fenrg.2024.1404386.
43. S. S. Rad, E. Nadi, M. Muhlbaier, O. Fishman, J. Chevinly, Z. Zheng, S. Zhao, F. Lu, and H. Zhang, "A novel cost-effective controller hardware-in-the-loop (CHIL) test for SSCB coordination in DC microgrid systems," IEEE Open J. Power Electron., pp. 1-9, 2024, doi: 10.1109/OJPEL.2024.3466188.